Fluoride-assisted detection of glutathione by surface Ce3+/Ce4+ engineered nanoceria

Vaishwik Patel, Linta Jose, Gilles Philippot, Cyril Aymonier, Talgat Inerbaev, Luke R Mccourt, Michael G Ruppert, Dongchen Qi, Wei Li, Jiangtao Qu, et al.

To cite this version:

Vaishwik Patel, Linta Jose, Gilles Philippot, Cyril Aymonier, Talgat Inerbaev, et al.. Fluoride-assisted detection of glutathione by surface Ce3+/Ce4+ engineered nanoceria. Journal of materials chemistry B, 2022, 10 (47), pp.9855-9868. 10.1039/D2TB01135B . hal-03907011

HAL Id: hal-03907011

https://hal.science/hal-03907011

Submitted on 19 Dec 2022

Fluoride-assisted detection of glutathione by surface Ce^{3+}/Ce^{4+} engineered nanoceria†

Vaishwik Patel,[a] Linta Jose,[a] Gilles Philippot,[b] Cyril Aymonier,[b]
Talgat Inerbaev,[cd] Luke R. McCourt,[e] Michael G. Ruppert,[e] Dongchen Qi,[f]
Wei Li,[f] Jiangtao Qu,[g] Rongkun Zheng,[g] Julie Cairney,[g] Jiabao Yi,[a]
Ajayan Vinu *[a] and Ajay S. Karakoti *[a]

Nanoceria has evolved as a promising nanomaterial due to its unique enzyme-like properties, including excellent oxidase mimetic activity, which significantly increases in the presence of fluoride ions. However, this significant increase in oxidase activity has never been utilised as a signal enhancer for the detection of biological analytes partly because of the lack of understanding of the mechanism involved in this process. In this study, we show that the surface oxidation state of cerium ions plays a very crucial role in different enzymatic activities, especially the oxidase mimetic activity by engineering nanoceria with three different surface Ce^{4+}/Ce^{3+} compositions. Using DFT calculations combined with Bader charge analysis, it is demonstrated that stoichiometric ceria registers a higher oxidase mimetic activity than oxygen-deficient ceria with a low Ce^{4+}/Ce^{3+} ratio due to a higher charge transfer from a substrate, 3,3′,5,5′ tetramethylbenzidine (TMB), to the ceria surface. We also show that the fluoride ions can significantly increase the charge transfer from the TMB surface to ceria irrespective of the surface Ce^{4+}/Ce^{3+} ratio. Using this knowledge, we first compare the fluoride sensing properties of nanoceria with high Ce^{4+} and mixed Ce^{4+}/Ce^{3+} oxidation states and further demonstrate that the linear detection range of fluoride ions can be extended to 1–10 ppm for nanoceria with mixed oxidation states. Then, we also demonstrate an assay for fluoride assisted detection of glutathione, an antioxidant with elevated levels during cancer, using nanoceria with a high surface Ce^{4+}/Ce^{3+} ratio. The addition of fluoride ions in this assay allows the detection of glutathione in the linear range of 2.5–50 ppm with a limit of detection (LOD) of 3.8 ppm. These studies not only underpin the role of the surface Ce^{4+}/Ce^{3+} ratio in tuning the fluoride assisted boost in the oxidase mimetic activity of nanoceria but also its strategic application in designing better colourimetric assays.

DOI: 10.1039//XXXXXXXXXX

Introduction

Fluoride ions have significant importance in human biological systems. They are associated with the prevention of dental caries, promotion, and growth of teeth, nails, bones, and hairs, and are beneficial in the treatment of osteoporosis. However, higher exposure to fluoride ions, slow excretion, and high adsorption in the human system result in dental fluorosis, kidney diseases, and gastric problems.[1] The World Health Organisation (WHO) and the United States Environmental Protection Agency (USEPA) have set the normal permissible limits of fluoride ions in drinking water at 1.0–1.5 ppm and 2–4 ppm, respectively.[2] Excessive fluoride exposure in humans arises from the consumption of fluorine-contaminated water, and an estimated 70 million people are affected by chronic exposure to high levels of fluoride ions.[3] Fluoride ions are also present in various fertilizers, resulting in their long-term accumulation in soil and groundwater.[4] Thus, it is important to detect and monitor the concentration of fluoride ions in various water sources. At present, fluoride ions are detected in the laboratory by using ion-selective electrodes or other techniques such as UPLC-MS,[5] LC-MS/MS,[6] HPLC,[7] ion chromatography,[8] ion specific electrodes,[9] ICP-OES,[10] electrochemical sensors,[11] microfluidic MOF sensors,[12] chemiluminescence[13] or fluorescence.[14] These methods require access to specialised instruments and require

---

[a] *Global Innovative Center for Advanced Nanomaterials (GICAN), School of Engineering College of Engineering, Science and Environment, The University of Newcastle, Callaghan, NSW, 2308, Australia.*
E-mail: ajayan.vinu@newcastle.edu.au, ajay.karakoti@newcastle.edu.au

[b] *Univ. Bordeaux, CNRS, Bordeaux INP, ICMCB, UMR 5026, F-33600 Pessac, France*

[c] *L. N. Gumilyov Eurasian National University, Nur-Sultan 010008, Kazakhstan*

[d] *National University of Science and Technology "MISIS", Moscow 119049, Russia*

[e] *School of Engineering, College of Engineering, Science and Environment, The University of Newcastle, Callaghan, 2308, Australia*

[f] *Centre for Materials Science, School of Chemistry and Physics, Queensland University of Technology, Brisbane, QLD 4001, Australia*

[g] *School of Physics, The University of Sydney, NSW, 2000, Australia*

† Electronic supplementary information (ESI) available. See DOI: **https://doi.org/10.1039/XXXXXXXXXX**

trained resources for their implementation, which is challenging for monitoring the concentration of fluoride ions at various sources of consumption. Thus, there is a need for the development of a sensitive and selective point of care (POC) detection of fluoride ions. In this regard, colourimetric detection of ions is one of the simplest and most user-friendly detection techniques capable of a qualitative and quantitative assessment of fluoride in drinking water. Several inorganic nanoparticles such as gold, silver or metal ion supplemented gold nanoparticles, or graphene oxide have been studied for the colourimetric detection of fluoride ions.[15,16] Researchers have also fabricated fluorescence based paper diagnostic tools for the visual detection of fluoride ions.[17,18] Although these materials show broad fluoride detection ability, the application of these materials is restricted due to their limited selectivity, low sensitivity and smaller range of detection of fluoride ions.[19]

Cerium oxide has recently gained significant attention in the colourimetric detection of fluoride ions among various materials. In its nano-sized form, the surface of cerium oxide nanoparticles (nanoceria) contains a mixture of Ce^{3+} and Ce^{4+} cations proportional to the number of surface oxygen vacancies.[20–23] The relative abundance of these oxidation states on the surface and its ability to switch between two different oxidation states imparts nanoceria with multiple biological enzyme mimicking activities.[24,25] Nanoceria has been shown to depict superoxide dismutase (SOD),[26] catalase,[27] oxidase,[28] and phosphatase enzyme-like activities[29] that can be used for the development of colourimetric sensors. Among these, oxidase-like activity has been used extensively for the detection of various analytes of biological and environmental significance, such as dopamine,[28,30] malathion,[31] alkaline phosphatase,[32] and cholesterol.[33,34] Recently, it was discovered that the oxidase mimetic activity of nanoceria can be modulated in the presence of fluoride ions.[35–37] This has led to the rapid development of colourimetric fluoride sensing technology based on nanoceria and its hybrids.[2,38,39] Liu and co-workers and others reported fluoride detection using the oxidase mimetic activity of nanoceria,[38] cerium zirconate nanocages,[2] and iron-ceria composites supporting the ability of nanoceria to interact with fluoride ions.[39] It must be noted that despite the high specificity and increased oxidase-like activity in the presence of F^-, the usage of CeO_2 in colourimetric biosensors is restricted because CeO_2 itself can oxidise the TMB dye and cause colour change. Hence, ceria-based fluoride sensing is not truly colourimetric at present because it is difficult to distinguish the colour change in the presence of fluoride ions and the detection is generally reported based on the rate of change of colour. Furthermore, the high initial oxidase activity of nanoceria limits the upper detection limit of fluoride ions and cannot be used for direct field sampling. Thus, there is a huge scope of improvement for tuning the nanoceria activity to increase the detection range of fluoride ions. Despite a number of reports, the mechanism surrounding the boost in the oxidase mimetic activity of nanoceria is still a matter of debate. Several mechanisms such as a facet dependent activity,[40] higher electronegativity or hard Lewis base nature of F^-[41,42] and recently, the increase in oxygen vacancy upon adsorption of the F^- ions on the surface of nanoceria[43] have been postulated. Despite these studies, detailed elucidation of the mechanism remains elusive. Surprisingly, the role of the oxidation state that is fundamental to the redox reactions has not been explored in detail for elucidating the oxidase mimetic activity or its boost in the presence of fluoride ions.

In this study, we depict a clear correlation between the surface oxidation state of nanoceria and its oxidase mimetic activity by engineering nanoceria with different surface oxidation states. Using first-principles calculations, we demonstrate that the TMB oxidation by nanoceria proceeds by the charge transfer from TMB to the nanoceria surface that increases with a decrease in surface Ce^{3+} concentration and the addition of fluoride ions. The theoretical predictions were validated experimentally by synthesizing nanoceria particles with three different ratios of surface Ce^{3+}/Ce^{4+} following three different synthesis protocols. It has been found that the oxidase mimetic activity decreased with increasing Ce^{3+} concentration and diminished completely for particles with the highest surface Ce^{3+}/Ce^{4+} concentration. The addition of fluoride ions increased the oxidase mimetic activity of nanoceria with the lowest Ce^{3+}/Ce^{4+} concentration but could not completely restore the diminished oxidase activity of nanoceria with the highest Ce^{3+}/Ce^{4+} ratio. We also demonstrate colourimetric detection of fluoride ions based on nanoceria with mixed surface Ce^{3+}/Ce^{4+} concentrations that show a significantly lower oxidation of TMB on its own. However, the oxidation is boosted in the presence of fluoride ions resulting in a visible colour change. Finally, we integrated the fluoride-based boost in the oxidase mimetic activity of nanoceria for designing an assay for the detection of glutathione, a cancer biomarker. This is the first time that the boosting ability of an analyte has been used in the sensitive detection of another analyte using nanoceria. By tuning the surface oxidation state of Ce ions, selective sensing of fluoride and glutathione was achieved with a lower detection limit of 0.6 ppm and 3.5 ppm, respectively.

Materials and methods

Materials

The materials used for the synthesis and testing of the enzymatic activity of nanoceria, such as ammonium cerium(IV) nitrate (ACN) (≥99.99%), cerium(III) nitrate hexahydrate (CNH) (99.99%), hydrogen peroxide (H_2O_2) (30% w/w), ammonium hydroxide (25%), cytochrome *C* (≥95%), xanthine oxidase (≥0.4 units per mg protein), hypoxanthine (99%), catalase (≥10 000 units per mg protein), tris HCl (reagent grade, ≥99.0%), diethylene triaminepentaacetic acid (DTPA) (99%), TMB (99%), sodium fluoride (99%), sodium hydrogen phosphate (99.998%), sodium chloride (≥99.0%), sodium bromide (≥99.0%), copper sulphate (≥99.0%), ammonium nitrate (≥99.0%), and reduced glutathione (≥98.0%) were purchased from Sigma Aldrich and used as received.

Synthesis of nanoceria with different surface oxidation states

Three different synthesis processes were selected for the synthesis of nanoceria with different surface oxidation states. At first, nanoceria with a higher surface Ce^{3+}/Ce^{4+} oxidation state ratio was synthesized using a wet chemical method following our previously well-established and characterised protocol.[44–46] In brief, 5 mM CNH was treated with 30% H_2O_2 and mixed thoroughly. The mixture was kept under ambient temperature and allowed to age for 15–21 days. Colour transformation from yellowish orange to colourless solution depicts the predominance of the Ce^{3+} oxidation state. This nanoceria was labelled as CeO-RT, representative of the predominance of the reduced form of cerium ions (Ce^{3+}) on the surface. The thermal hydrolysis method was selected for the synthesis of nanoceria with a low Ce^{3+} oxidation state, which generally yields ∼10–15% surface Ce^{3+} concentration. Briefly, 100 mM ACN was hydrolysed by 5 N NH_4OH at 65 °C. The synthesised particles were purified by dialysis to remove unreacted precursor ions and increase the pH of the solution to 3.0.[47] These particles were labelled as CeO-TH, representative of the predominance of the oxidized form of cerium ions (Ce^{4+}) on the surface. Nanoceria with a mixed oxidation state was prepared with a supercritical flow process temperature following previously established protocols with slight modification.[48,49] In brief, a 10 mM ACN solution was prepared by dissolving the precursor in absolute ethanol. This solution was later injected with a high-pressure pump into a five-meter-long tubular reactor (1/8″ inch stainless steel). The reactor was heated at 300 °C and pressurized at 25 MPa to reach the supercritical conditions of ethanol (T_{crit} = 240.8 °C; P_{crit} = 6.1 MPa).[48] The flow rate was adjusted to have a residence time of 55 seconds in the hot and pressurized zone of the reactor. Downstream, the medium was quenched with an ice bath, and the nanoceria was recovered in suspension upon depressurization through a back pressure regulator valve. The powder was later filtered and dried. The particles synthesized by this method were labelled as CeO-SC, representative of the mixed oxidation states relative to the CeO-RT and CeO-TH nanoparticles used in this study. Note that the use of ACN or CNH as precursors and ammonia and hydrogen peroxide as oxidizing/hydrolysis agents results in the synthesis of particles without any organic functional groups on the surface. Thus, all the properties observed in this study can be ascribed directly to nanoceria and the relative oxidation states of the cerium ions on the surface.

Characterization

The optical properties, indicative of the oxidation state of cerium ions in nanoceria suspensions, were studied by measuring the absorbance of the as-synthesized nanoparticles using a PerkinElmer Lambda 365 UV-Visible spectrophotometer with a 150 nm min^{-1} scan rate. The particle size in the solution following the synthesis was analysed by a FEI Themis Z double-corrected S/TEM operating at 300 kV accelerating voltage. For TEM measurements, the as-synthesized particles in solution were directly drop casted on a holey carbon coated copper grid. The photoluminescence (PL) activity of the particles was measured with a PerkinElmer LS 55 fluorescence spectrometer instrument. For fluorescence measurements, the particles were excited at a wavelength of 255 nm, and emission was observed in the range of 300–450 nm (max emission at ∼355 nm). The X-ray diffraction (XRD) patterns were obtained by using a Panalytical Empyrean diffractometer operated with CuKα1 (1.5405 Å) and Kα2 (1.5444 Å) radiations along with a voltage of 40 kV and tube current of 40 mA to identify the crystallinity of the particles synthesized by different methods. The presence of surface oxygen vacancies was confirmed by Raman spectroscopy (Horiba XploRA Confocal Raman microscope) by using a 532 nm laser light for sample excitation. Data were collected at room temperature with 2400 grooves/mm grating. The surface oxidation states of cerium ions in different nanoceria before and after incubation with fluoride ions were studied by X-ray photoelectron spectroscopy with a Kratos AXIS Supra photoelectron spectrometer using a monochromatized Al K_a X-ray source.

Assessment of enzyme mimicking activities of nanoceria

SOD mimetic activity was carried out by following the method developed by Korsvik *et al.*[26] This method is based on the reduction of cytochrome *C*, stimulated by superoxide radicals generated in the assay by the reaction of xanthine oxidase and hypoxanthine. Nanomaterials with SOD mimetic activity neutralize the superoxide radicals and prevent the reduction of ferricytochrome *C* to ferrocytochrome *C*, which can be monitored by measuring its time-dependent change in the absorbance. The reduction of cytochrome *C* by various nanoceria preparations at a concentration of 250 μM was analyzed by measuring the absorbance of ferrocytochrome *C* at 550 nm in 96 well plates with a final volume of 100 μL using a Varioskan LUX microplate reader (Thermo Fisher). Catalase was added to the assay to remove the oxidative by-products formed by the reaction of nanoparticles with superoxide radicals.

The catalase mimetic activity of nanoceria was assessed by following the method developed by Pirmohmmad *et al.*[27] Nanoceria catalysed degradation of H_2O_2 into H_2O and O_2 is monitored by measuring the reduction in the absorbance of H_2O_2 at 240 nm using a PerkinElmer Lambda 365 UV-Visible spectrophotometer. Tris-HCl was added to maintain the pH of the reaction system (∼6.8) and DTPA was used as a chelating agent to arrest the oxidation state of the nanoparticles and testing was carried out using a 250 μM concentration for all three types of nanoparticles. The oxidase mimetic activity of the nanoceria samples was assessed by following the method described by Asati *et al.*[28] Briefly, an increase in the absorption of the oxidized TMB (blue colour) following a single point oxidation of 1 mM TMB (colourless) at acidic pH (0.1 M acetate buffer) by nanoceria was analysed by monitoring the absorbance at 652 nm using a Varioskan LUX microplate reader.

Assessment of fluoride ions and glutathione

Biosensing of fluoride and glutathione was carried out by using the oxidase mimetic activity of nanoceria described above. In brief, the oxidase activity of different nanoceria samples, specially CeO_2-TH and CeO_2-ST, was assessed in the presence of different fluoride concentrations (0.5, 0.75, 1.0, 2.0, 4.0, 6.0, 8.0 and 10.0 ppm) and further repeated for consistency. In all samples, fluoride was added to the assay with TMB followed by the addition of nanoceria. Glutathione, a well-known antioxidant, was used to quench the oxidase mimetic activity of CeO_2-TH and this was used as an indirect assay for sensing glutathione. The oxidase mimetic activity of CeO_2-TH (500 μM) in the presence of different concentrations of glutathione (1, 2.5, 5.0, 10.0, 15.0, 20.0, 25.0, 40.0, and 50.0 ppm) was measured to determine the linear range of response. Fluoride ions were then added at a fixed concentration of 1 ppm in the assay to increase the higher range of detection of glutathione. The concentration of respective analytes was assessed based on the change in the oxidase mimetic activity in the presence of fluoride ions and glutathione.

DFT calculations

All calculations were carried out with the plane-wave based Vienna ab initio simulation package (VASP).[50,51] The geometry optimisation of the electronic ground state was performed using local density (LDA+U) approximation. On-site Coulomb and exchange interaction were treated by a single effective parameter $U_{\text{eff}} = U - J$.[52] Plane waves energy cut off of 500 eV, projected augmented wave (PAW) method,[53] and $U_{\text{eff}} = 5$ eV was used. It was previously shown that this method most accurately describes the process of vacancy formation in nanoceria.[54–57]

Results and discussion

Surface and bulk properties of nanoceria particles (CeO-RT, CeO-TH and CeO-SC) with different surface Ce^{3+}/Ce^{4+} oxidation state ratios were characterized with various tools including powder XRD, HRTEM, and UV-Visible, photoluminescence and Raman spectroscopy to determine the particle size, crystalline state, presence of surface oxygen vacancies, and relative oxidation states and the results are shown in Fig. 1. The crystallite size of nanoceria particles synthesized using all three methods was analysed by high-angle annular dark-field (HAADF) imaging under STEM mode and was found to be within the 3–5 nm range, as shown in Fig. 1a–c. It is apparent that the size of CeO-RT and CeO-TH particles is slightly smaller (3–4 nm) as compared to that of CeO-SC (4–5 nm). All the

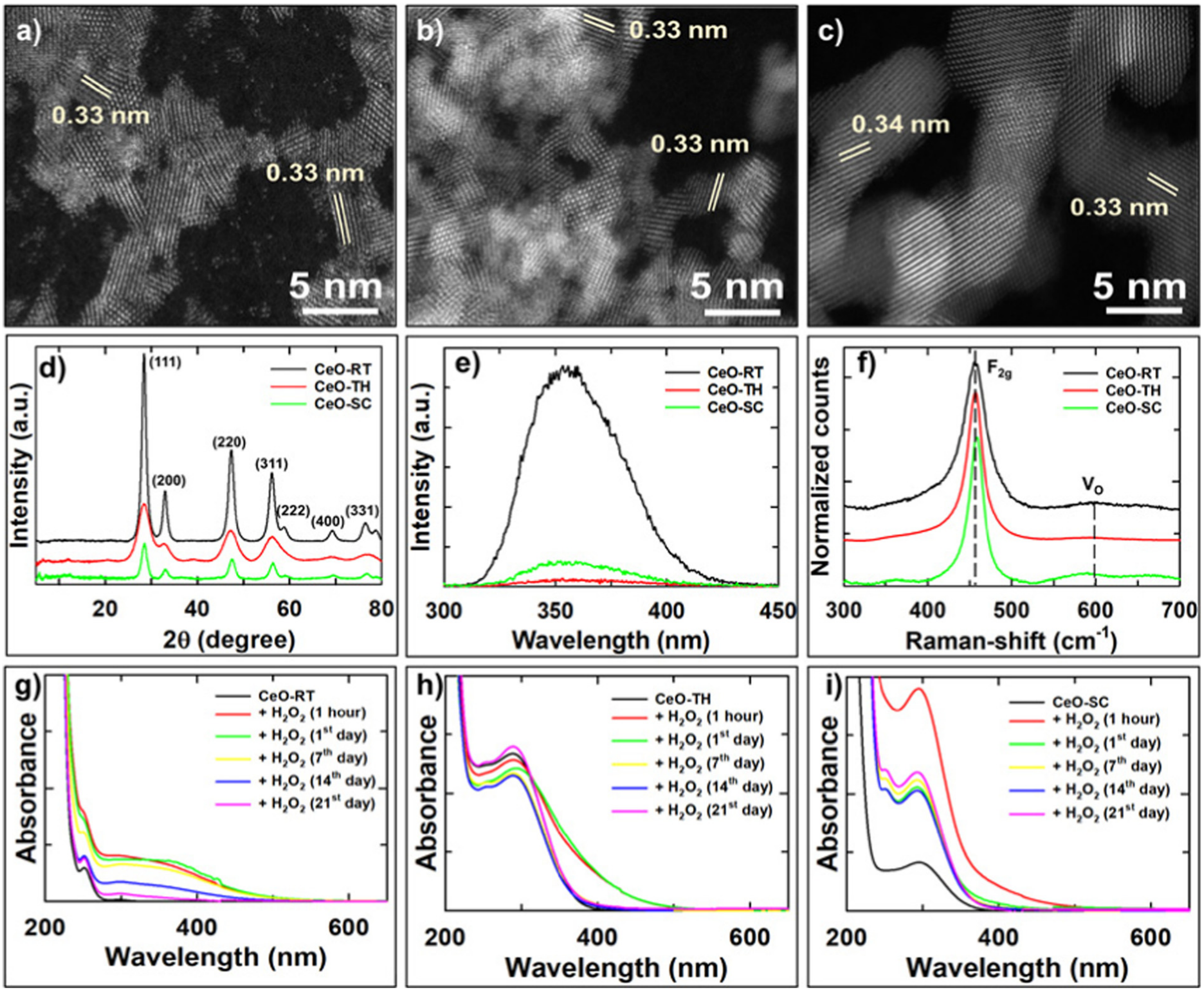

Fig. 1 Characterization of nanoceria prepared by different methods. STEM-HAADF images indicate nanosized (a) CeO-RT, (b) CeO-TH, and (c) CeO-SC; (d) XRD results indicate the structural similarity between the samples; (e) PL data indicate the higher luminescence intensity of CeO-RT as compared to CeO-SC and CeO-TH; (f) Raman spectra of the samples indicate the F_{2g} phonon and the defect peak; UV-Visible spectra and autocatalytic activity of (g) CeO-RT, (h) CeO-TH, and (i) CeO-SC.

samples depicted good crystallinity with visible lattice fringes corresponding to the (111) planes of cerium oxide. The crystallinity of the samples was further analysed by XRD. The XRD diffraction patterns of all three samples show almost similar peaks corresponding to the fluorite lattice of cerium oxide (Fig. 1d). The major peaks located at 2θ values of 28.5, 33.1, 47.2 and 56.3 degrees, correspond to the (111), (200), (220) and (311) crystal planes, respectively, confirming that all samples depict the formation of nanocrystalline cerium oxide. The PL study was carried out to compare the electronic properties of different samples. Ce^{3+} ions show an inherent 5d → 4f electronic transition, which is observed as a characteristic peak around 355 nm using an excitation wavelength of 255 nm.[58] This PL peak is exclusive to the presence of the Ce^{3+} oxidation state in nanoceria. It can be observed from Fig. 1e that the CeO-RT shows a characteristic PL peak centred at 355 nm. In comparison, no PL peak is observed for CeO-TH while CeO-SC shows a weak PL peak upon excitation. Thus, it is evident from the PL measurements that CeO-RT exhibits a higher ratio of Ce^{3+}/Ce^{4+} while CeO-TH possesses a minimal ratio of Ce^{3+}/Ce^{4+} ions. In comparison, CeO-SC shows some PL activity, suggesting that the surface Ce^{3+}/Ce^{4+} ratio is lower than CeO-RT but higher than CeO-TH.

Raman spectroscopic measurements were conducted to confirm the presence of surface oxygen vacancies in the samples. Cerium oxide shows a prominent Raman peak at 465 cm^{-1} corresponding to the F_{2g} phonon mode due to the symmetrical stretching of the oxygen anions around the cerium cations. This Raman mode is sensitive to the sub-structure and disorder around the oxygen ions and results in a blue shift of the peak for nanoceria as compared to bulk cerium oxide concomitant with the decrease in the phonon lifetime. The Raman spectral investigations show that CeO-RT, CeO-TH and CeO-SC depict broad Raman peaks at 455.4 cm^{-1}, 456.5 cm^{-1} and 458.6 cm^{-1}, respectively (Fig. 1f). The blue shift in the peak positions confirms the nanocrystalline nature of the samples. In addition to the sharp and major phonon peak ($\sim$465 cm^{-1}), the presence of a small peak between $\sim$570 and 600 cm^{-1} is ascribed to the presence of oxygen vacancies in the ceria lattice. It is observed from Fig. 1f that CeO-RT and CeO-SC samples depict a broad peak in this region, confirming the presence of surface oxygen vacancies, while the CeO-TH sample depicts a minor peak, suggesting that this sample contains fewer surface oxygen vacancies.[59,60]

At first, the redox activity of nanoceria was tested by following the cyclic reversibility of the oxidation states of nanoceria following their exposure to hydrogen peroxide using UV-Vis spectroscopy. Nanoceria has been shown to react reversibly with hydrogen peroxide in a slow, time-dependent manner *via* the formation of an intermediate cerium-oxo-peroxo compound that clearly shows a change in the optical absorption spectra based on the particle size and Ce^{3+}/Ce^{4+} ratio.[44,45,61–63] The UV-Vis spectra of CeO-RT, CeO-TH and CeO-SC following their interaction with hydrogen peroxide (0.1 mL) are shown in Fig. 1g–i. It is observed that CeO-RT shows a λ_{max} at 255 nm while both CeO-TH and CeO-SC show a $\lambda_{max} \sim 300$ nm, suggesting that the CeO-RT particles contain a higher ratio of Ce^{3+}/Ce^{4+} as compared to the other two particles. The effect of the addition of H_2O_2 on the formation of the cerium-oxo-peroxo complex was followed by time-dependent absorbance measurements as well as by visibly observing the changes in the colour of the suspension (ESI-1†). It is observed that the addition of H_2O_2 induces a colour change in all three samples that slowly changes back to the original colour after 14–21 days of incubation (ESI-1†). The change in colour is consistent with the previous reports[64,65] and is ascribed to the formation of the metastable cerium-oxo-peroxo compound and its slow decomposition in solution with the evolution of oxygen. This also results in the transition of surface Ce^{3+}/Ce^{4+} to primarily Ce^{4+} and regeneration of the original Ce^{3+}/Ce^{4+} concentration in a cyclic manner. The time-dependent changes in the UV-visible absorption spectra of the samples are shown in Fig. 1g–i. It is observed that the addition of H_2O_2 results in an increase in the absorbance value for all the samples in the 300–500 nm region of the spectrum, confirming the formation of the cerium-oxo-peroxo compound though the maximal change is observed for CeO-RT followed by CeO-SC and the smallest change is observed for the CeO-TH. Upon aging for 21 days, the absorbance in the 300–500 nm range disappeared, and the original spectrum of the nanoceria sample is regenerated, indicative of the amount of surface Ce^{3+}/Ce^{4+} ratio in these samples. Unlike CeO-RT and CeO-TH, CeO-SC showed a notably slow regeneration of its original spectrum as well as the emergence of a characteristic peak at 255 nm in addition to the 300 nm peak, revealing that the regenerated surface has a higher ratio of Ce^{3+}/Ce^{4+} as compared to the pristine surface before the addition of H_2O_2. These results suggest that all three ceria samples show reversible redox activity with hydrogen peroxide and are suitable to depict enzyme mimetic activity. The optical absorbance spectra are consistent with the PL, Raman and XPS data, suggesting the presence of a high, low and mixed Ce^{3+}/Ce^{4+} ratio in CeO-RT, CeO-TH and CeO-SC samples.

XPS analysis was conducted to quantify the oxidation states of cerium in all the samples. The core level Ce 3d photoelectron spectra from all the samples are shown in the ESI-2.† The Ce 3d core-level spectra consist of multiple peaks arising from the spin–orbit coupling of Ce $3d_{3/2}$ and Ce $3d_{5/2}$ orbitals as well as the presence of various shake-up and shake down peaks. It is known that the peaks corresponding to Ce^{4+} ion appear around 882, 888, 898, 900, 907 and 916 eV, whereas peaks around 880, 884, 899 and 903 eV indicate the predominance of Ce^{3+} ions. XPS analysis indicates that CeO-TH shows a predominant presence of Ce^{4+} ions while CeO-RT exhibits a dominant presence of Ce^{3+} ions on the surface. The surface Ce^{3+} concentration of the CeO-SC sample, on the other hand, is lower than CeO-RT but higher than the CeO-TH sample. The curve-fitting of the spectra was conducted and the amount of Ce^{4+} in the samples was estimated based on ((1 − (area of Ce^{3+} oxidation state/area of total Ce oxidation states)) × 100). The concentration of the surface Ce^{4+} ions was found to be 34%, 88% and 80% in the CeO-RT, CeO-TH and CeO-SC samples, respectively (ESI-3†). Hence, based on the characterisation data, the samples synthesized by three different methods show different amounts of surface Ce^{3+}/Ce^{4+} ratio and are ideal candidates to test the effect of oxidation states on the enzymatic activity of nanoceria.

Assessment of the enzyme mimetic activities

The effect of different surface Ce^{3+}/Ce^{4+} ratios in the three samples on the enzyme mimetic activity was assessed using SOD, catalase and oxidase mimetic assays. The assessment of enzymatic activities was conducted using well-established cell-free *ex vitro* methods. The SOD mimetic activity tests the ability of nanoceria to scavenge superoxide radicals generated by the hypoxanthine/xanthine oxidase system. The reduction of ferricytochrome *C* by superoxide radicals is marked by a change in the colour of the solution from reddish-orange to pink and can be measured using a multi-well plate reader at 550 nm. A time-dependent increase in the absorbance at 550 nm reflects the presence of a higher concentration of superoxide radicals (blank in Fig. 2a). It is observed from Fig. 2a that CeO-RT and CeO-SC prevent the reduction of ferricytochrome *C*, depicting a high SOD activity, while CeO-TH shows only mild SOD activity as compared to the blank sample. The SOD activity of nanoceria is directly related to the surface Ce^{3+}/Ce^{4+} concentration and nanoceria with a high Ce^{3+}/Ce^{4+} ratio is known to have high SOD activity.

Thus, it can be concluded that both CeO-RT and CeO-SC have a higher surface Ce^{3+}/Ce^{4+} ratio as compared to CeO-TH, which is consistent with the characterisation data. Furthermore, the catalase mimetic activity of samples was analysed by following previously developed protocols.[66] It is observed in Fig. 2b that CeO-TH and CeO-SC show a high catalase activity while the CeO-RT sample did not have any catalase activity. Our and other groups have shown that nanoceria with low Ce^{3+}/Ce^{4+} ratios demonstrate a high catalase activity, although recent studies have indicated that nanoceria with mixed oxidation states on the surface also show a high catalase activity. These results suggest that CeO-RT with a high Ce^{3+}/Ce^{4+} ratio cannot decompose H_2O_2 as compared to CeO-TH, which has a low Ce^{3+}/Ce^{4+} ratio. The high catalase activity depicted by CeO-SC shows that this sample probably has mixed oxidation states that are higher than CeO-TH but lower than CeO-RT. These results also support previous studies where mixed oxidation state nanoceria has been shown to depict higher catalase mimetic activities.[61,67]

The role of oxidation states on the oxidase mimetic activity was also tested by measuring the direct oxidation of TMB by different samples of nanoceria. TMB dye possesses two amine groups and can undergo two-point oxidation. Oxidation of one amine group results in a colour change from colourless to blue while it changes to yellow if both the amine groups are oxidized. The single point oxidation of TMB and the rate of oxidation can be evaluated by measuring the time-dependent

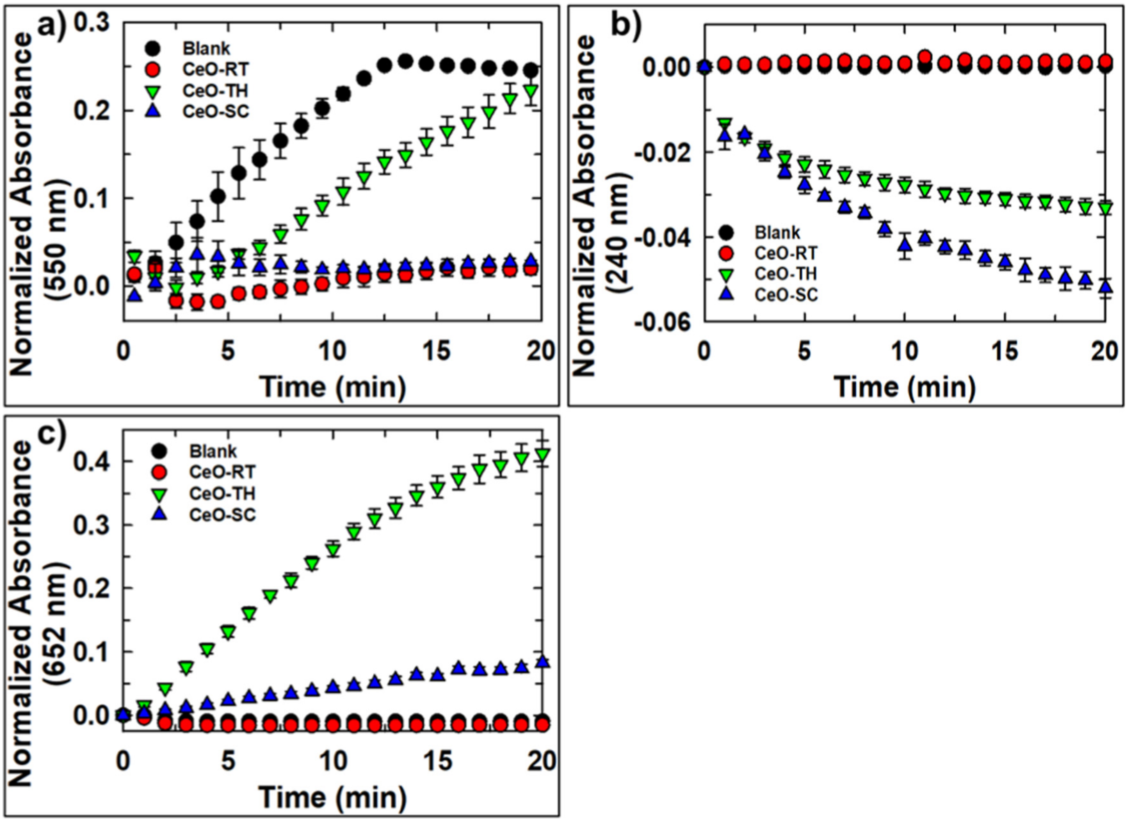

Fig. 2 Comparison of enzymatic activities of nanoceria samples with different surface oxidation states. (a) SOD mimetic activity (normalised absorbance at 550 nm), (b) catalase mimetic activity (normalised absorbance at 240 nm) and (c) oxidase mimetic activity (normalised absorbance at 652 nm) (concentration of nanoparticles: 250 μM).

increase in the absorbance of TMB oxidation at 652 nm. As depicted in Fig. 2c, CeO-TH shows the highest oxidase mimetic activity, followed by CeO-SC, which shows a mild activity, while CeO-RT does not show any oxidase mimetic activity. Thus, our experimental data reveal that the oxidation state of cerium ions on the surface of nanoceria is the most important factor, which is clearly depicted by the lack of oxidase mimetic activity in the CeO-RT sample with the highest Ce^{3+}/Ce^{4+} ratio. This result is in direct agreement with the theoretical charge transfer analysis (described later), which showed a reduction in the charge transfer from TMB to cerium oxide slab with increasing Ce^{3+} concentration. The increase in surface Ce^{3+} concentration increases the overall electron density over the nanoceria surface, thereby reducing its ability to accept electrons from (or oxidize) the TMB. It is interesting to note the difference in the oxidase mimetic activity of CeO-SC and CeO-TH. Even though the Ce^{3+} concentration in CeO-SC is only slightly higher (~18%) as compared to CeO-TH (~10%), its oxidase activity decreases drastically, suggesting a large influence of Ce^{3+} ions on the oxidizing ability of nanoceria. The most interesting enzyme mimicking behaviour among all samples is noted for CeO-SC as it shows excellent SOD, catalase, and mild oxidase mimetic activities. The mild oxidase-like activity of this sample suggests that even though CeO-SC possesses both Ce^{3+} and Ce^{4+} ions on the surface, there are neither enough surface Ce^{3+} ions to completely block the oxidase mimetic activity nor enough Ce^{4+} ions to depict a high oxidase mimetic activity. Note that all three nanoceria samples were synthesized using chemically similar precursors (cerium nitrate hexahydrate and ammonium cerium nitrate) and the oxidizing/hydrolysing agents used in the study (H_2O_2 and ammonia) are good leaving agents. Hence, the effect of the enzymatic activity can be ascribed directly to the surface oxidation states of cerium ions without the influence of adsorbed impurities. Based on the results, CeO-TH and CeO-RT were selected for testing the effect of fluoride ions on their oxidase mimetic activity and sensing ability for fluoride ions.

Effect of oxidation state on the fluoride sensing

We evaluated the potential of fluoride ions to boost the oxidase mimetic activity of nanoceria samples with different surface oxidation states by measuring the activity in the absence and presence of fluoride ions. Fig. 3a and b show the concentration-dependent oxidase mimetic activity of nanoceria samples (CeO-TH and CeO-SC, respectively) in the absence of fluoride ions. It is observed that the oxidase mimetic activity increases with an increase in the concentration of both nanoceria samples, as reflected in the corresponding increase in the absorbance values. As the concentration of nanoceria samples increases in the assay, more surface Ce^{4+} sites are available to oxidize the TMB. Furthermore, the effect of increasing the concentration of fluoride ions on the oxidase mimetic activity of the optimised concentration (500 μM) of nanoceria was analysed for its application as a fluoride sensor. It is noted that fluoride ions cannot carry out the oxidation of TMB by themselves in the concentration range tested in this study (ESI-4a†). The concentration of fluoride ions was varied between 1–10 ppm to stay slightly above and below the WHO recommended limit of 4 ppm of fluoride ions in water. It is observed from Fig. 3c that the oxidase mimetic activity of CeO-TH increases significantly with an increase in the concentration of fluoride ions. However, the activity is saturated beyond 2 ppm, and no further increase in the reaction rate or the absorbance is observed for 3 and 4 ppm fluoride concentrations. In comparison, for the same concentration of CeO-SC sample, a similar increase in the oxidase activity is observed with an increase in the fluoride concentration; however, in this case, the absorbance is not saturated up to 10 ppm of fluoride (Fig. 3d). This observation suggests that the CeO-TH is a better sample for detecting a lower concentration of fluoride ions (0.5–2 ppm). However, CeO-SC is better for detecting fluoride in a broader range from 1–10 ppm, especially in the range above the WHO recommended limit. The linear range of detection of fluoride for CeO-SC is shown in the ESI-4b.† It was also observed that both the samples showed high selectivity towards 4 ppm fluoride ions, as depicted in Fig. 3e and f. From the inset (Fig. 3e and f), it is also observed that CeO-SC is a better colourimetric sensor for the visual detection of fluoride. Due to an inherently low oxidase activity of CeO-SC, the TMB dye in the assay is not oxidized by nanoceria alone and the solution is nearly colourless. However, in the presence of 4 ppm fluoride ions the characteristic blue colour of the oxidized TMB is much easier to detect. In contrast, CeO-TH shows a visible colour change from blue to dark blue in the presence of fluoride that is visually harder to detect (inset image in Fig. 3e). The steady-state kinetics of the TMB oxidation by CeO-SC and CeO-TH reaction in the presence and absence of fluoride ions followed Michaelis Menten kinetics and the kinetics parameters extracted from the Lineweaver–Burk plots[68] are depicted in the ESI-5.† Enzyme kinetics data indicate that the K_m (Michaelis constant) value decreases from 0.56 and 10.99 to 0.18 and 1.2 after the addition of 4 ppm fluoride ions for CeO-TH and CeO-SC, respectively. The decrease in K_m values indicates that fluoride ions increase the affinity of both CeO-TH and CeO-SC towards TMB though the decrease in the K_m value is significantly higher for CeO-SC as compared to CeO-TH. A corresponding increase in the V_{max} values was also observed from 2.6×10^{-7} M s^{-1} to 5.4×10^{-7} M s^{-1} for CeO-TH samples, while it increased from 6.98×10^{-8} M s^{-1} to 9.25×10^{-8} M s^{-1} for CeO-SC samples in the absence and presence of fluoride ions, respectively. It can also be observed from Fig. 3c and d that even though the fluoride ions can boost the oxidation of TMB by nanoceria, a saturation of the activity is observed at lower fluoride concentration (2 ppm) for CeO-TH which possesses higher surface Ce^{4+} ions. The oxidase assay contains about 1 mM TMB and hence the saturation in its enzymatic activity cannot occur due to the complete consumption of the TMB dye in the assay. The saturation of nanoceria activity is ascribed to the adsorption of oxidized TMB product on the surface, which blocks the access of the free TMB molecules to the active Ce^{4+} sites.[69] Recently, Zhao *et al.* showed this effect by reacting nanoceria with a high concentration of TMB and ABTS (2,2 Azino-bis(3-ethylbenzothiazoline-6-sulfonic acid)) dye as a substrate.[42] It was further shown that the adsorption of fluoride ions on the surface

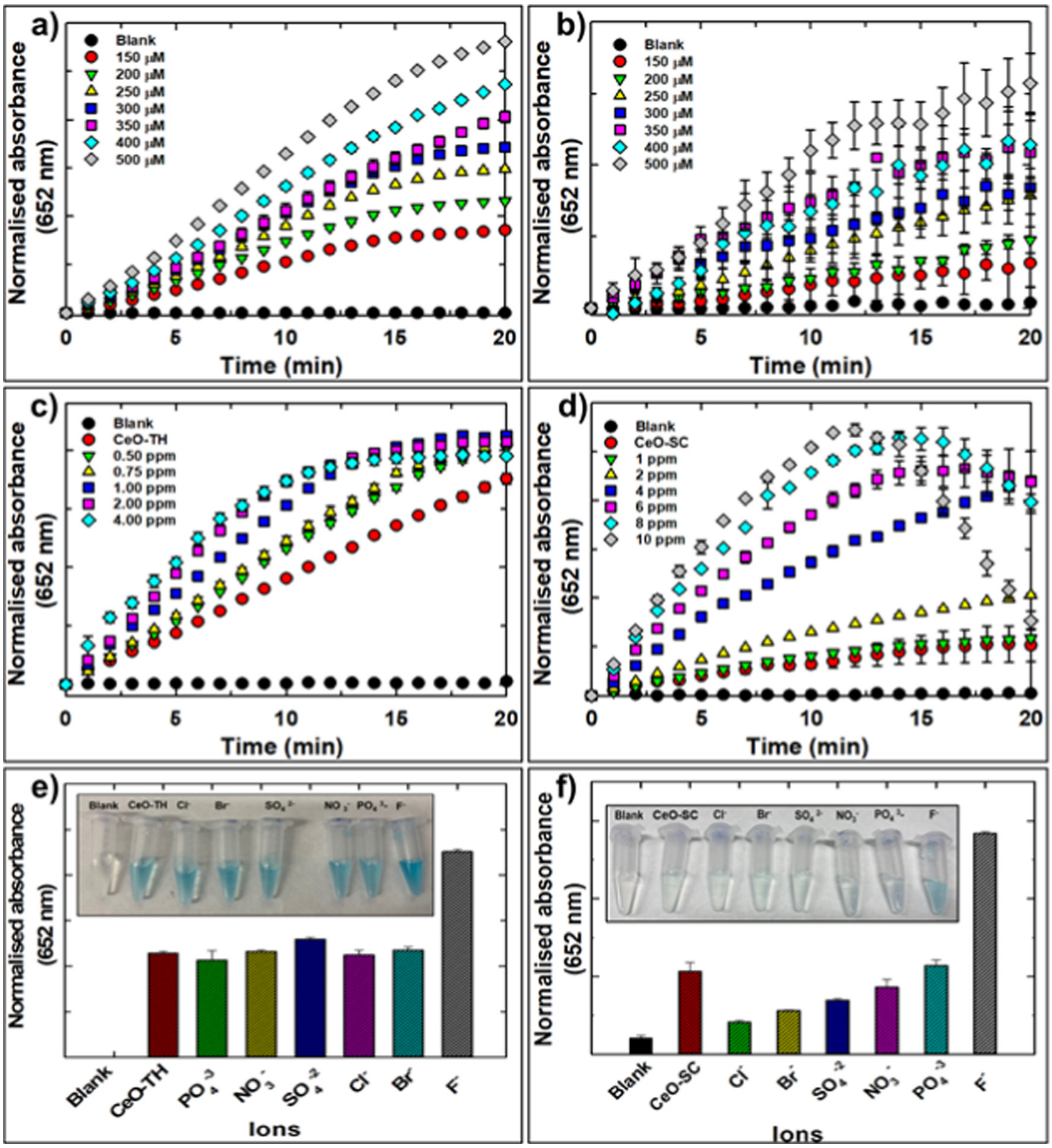

Fig. 3 Concentration dependent oxidase mimetic activity of (a) CeO-TH and (b) CeO-SC samples; oxidase mimetic activity of (c) CeO-TH and (d) CeO-SC in the presence of different concentrations of fluoride ions; selectivity of sensing of (e) CeO-TH and (f) CeO-SC toward fluoride ions.

of nanoceria results in reversing the zeta potential of the nanoceria to negative values. The electrostatic repulsion between the negatively charged nanoceria surface and the oxidized dye promotes its desorption which was cited as one of the mechanisms for the observed boost in the oxidase mimetic activity of nanoceria by fluoride ions. While these results are obtained for nanoceria with a large number of adsorbed fluoride ions by exposing nanoceria to a high fluoride concentration (5 mM), our results obtained at significantly lower concentrations (0.5–10 ppm) show that the mechanism may also be influenced by the concentration of surface Ce^{3+} ions in addition to the amount of adsorbed fluoride ions. The zeta potential measurements also did not show any significant differences in the samples (ESI-6†). In the current experiments, a saturation of the oxidase activity of a fixed concentration of nanoceria (500 μM) in the presence of an increasing concentration of fluoride ions suggests that desorption of TMB by fluoride ions can not be the main mechanism of the observed boost in its oxidase activity at this low concentration. If fluoride ions promoted desorption, then the oxidase activity should have increased with increasing fluoride concentration. We hypothesize that the presence of slightly higher surface Ce^{3+} in CeO-SC may facilitate the desorption of the oxidized TMB from the surface and further allow more TMB molecules to access the surface by influencing the orientation of the adsorbing TMB molecule. Thus, the activity CeO-SC with higher Ce^{3+} is not saturated at a higher fluoride concentration as it can accommodate relatively higher TMB molecules on its surface compared to

CeO-TH. It is of note that Zhao *et al.* showed an increase in the concentration of surface Ce^{3+} concentration after exposure to 5 mM fluoride, which may have also influenced their results.[42] The influence of fluoride ions on the oxidation state of CeO-SC and CeO-TH before and after exposure to 4 ppm fluoride was analysed by XPS. The cerium 3d core level X-ray photoelectron spectra of CeO-TH and CeO-SC after treatment with fluoride ions are shown in Fig. 4. The deconvolution of the spectra followed by the quantification of surface Ce^{4+} (ESI-3†) show a negligible change in the concentration of Ce^{3+} ions after exposure to fluoride ions for both the samples. The Ce^{3+} content in the CeO-TH remained unchanged while it is changed from 20.33% to 18.76% in CeO-SC after exposure to fluoride ions. The low concentration of fluoride ions used in this experiment is unable to cause a significant change in the oxidation states of surface cerium ions. This suggests that the native Ce^{3+}/Ce^{4+} oxidation state ratio is unchanged in these samples and may directly influence the saturation kinetics of TMB oxidation instead of fluoride ions. Our results unambiguously demonstrate that the oxidation state of nanoceria has a significant role in the oxidase mimetic activity of nanoceria and its increase in the presence of fluoride ions. The fluoride ions can facilitate the charge transfer from TMB to nanoceria owing to their high electronegativity. DFT calculations were performed and analysed using Bader analysis[70] to understand the role of fluoride ions in the charge transfer from TMB to the nanoceria surface.

In oxidase mimetic activity, the cerium ions on the surface of nanoceria act as an oxidizing agent by accepting the electrons from the TMB molecules resulting in the oxidation of the latter. Thus, we compared the charge transfer from TMB to a ceria surface with and without the surface oxygen vacancies. For comparison, a $CeO_2(111)$ slab consisting of 9 atomic layers and 144 atoms (48 cerium and 96 oxygen atoms) was designed to create a stoichiometric ceria slab. This configuration was selected since the ceria (111) surface is the most energetically favourable.[71,72] We considered a slab geometry with a vacuum layer of thickness 15 Å added to the simulation cell to simulate a surface. The non-stoichiometric ceria slab contained 48 cerium atoms and 94 oxygen atoms. The two oxygen vacancies were created by removing oxygen atoms (highlighted in blue – in stoichiometric ceria slabs in Fig. 5), resulting in the reduction of four surface cerium ions. In order to analyse the interaction between the ceria slab and the TMB molecules, one TMB molecule was placed on each side within the proximity of the ceria and the resulting system was optimized to an equilibrium position (Fig. 5a–c). Similarly, the charge transfer from the stoichiometric ceria slab and the slab with oxygen vacancies in the presence and absence of two F^- was also analysed. Two possible cases were considered for the adsorption of F^- ions. In the first, the equilibrium positions of the F^- ions were determined by optimizing the system's geometry under consideration (fully relaxed structure). In this case, the F^- ions were located at a distance of 2.12 Å above the surface Ce^{4+} ions. In the second case, the positions of F^- ions were fixed at a distance of 5 Å above the surface of cerium oxide (selective dynamics calculations). The positions of other atoms were determined in the relaxation of atomic coordinates. When F^- ions are adsorbed on the surface of cerium oxide, the charge transfer is more significant since the charge state of the F^- ion remote from the surface is $-0.8\ |e|$, while that of the adsorbed one is $-0.7\ |e|$. Thus, the CeO_2 slab takes a part of the electron density from the F^- ion, indicating that F^- ions can mediate the electron transfer between ceria and TMB.

The charge distribution was analysed using Bader charge analysis[70] and the results are presented in Table 1. Fig. 5d represents charge density differences [Charge (CeO_2-TMB) − {Charge(CeO_2) + Charge(TMB)}] between the sum of the independent charges of perfect CeO_2 slab and TMB molecules and the TMB adsorbed on CeO_2. Cyan colour represents a reduced charge density in a specific region of space for the CeO_2 + TMB structure compared with the same value for the sum of the charge densities of the CeO_2 slab and TMB molecule, while yellow represents an increased charge density. The increasing cyan colour on the TMB molecule suggests a charge transfer from the adsorbed TMB molecules to the stoichiometric cerium oxide slab. However, the charge transfer reduces to almost half (of the value obtained for a perfect slab) in the presence of

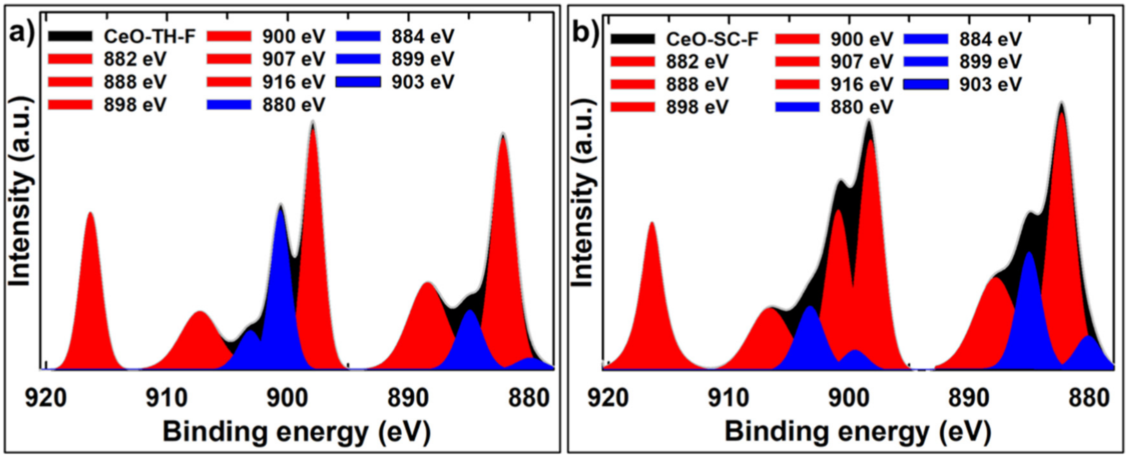

Fig. 4 Deconvoluted 3d core level XPS spectra of (a) CeO-TH and (b) CeO-SC after exposure to low concentrations of fluoride ions.

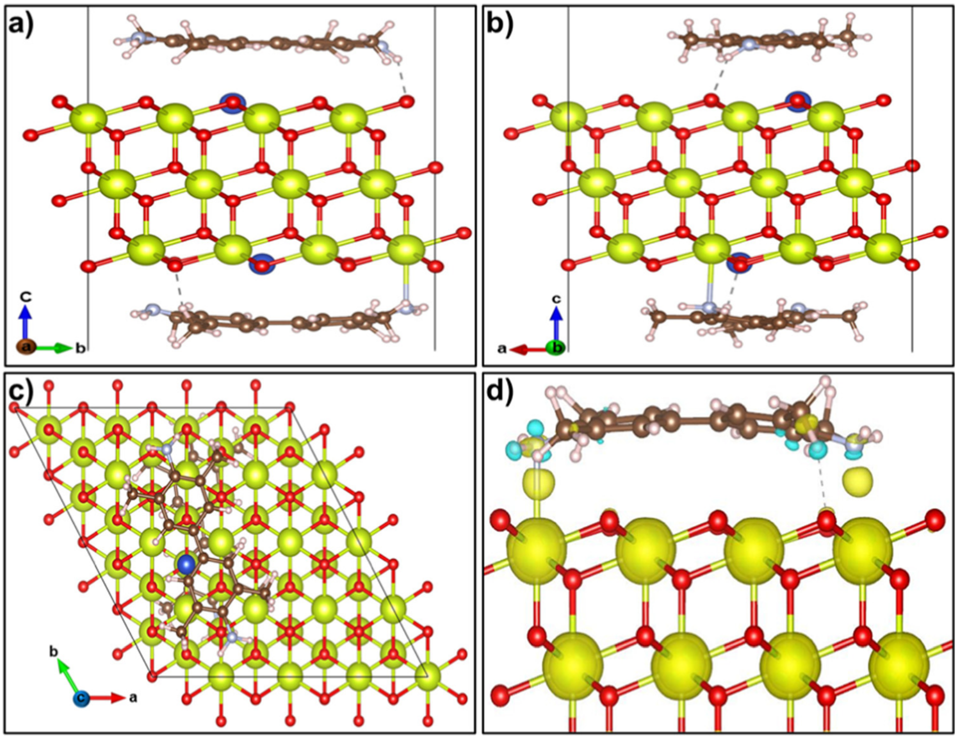

Fig. 5 Representation of the TMB adsorption on a stoichiometric (perfect) $CeO_2(111)$ slab (a and b) side view and (c) top view, the blue colour oxygen were removed to create vacancies for creating non-stoichiometric (defective) ceria; (d) charge density difference for the favourable adsorption configuration of TMB on the stoichiometric $CeO_2(111)$ surface calculated as $q(CeO_2 + TMB)-[q(CeO_2) + q(TMB)]$. Yellow and cyan clouds represent charge gain and loss, respectively.

oxygen vacancies on the surface of non-stoichiometric ceria. This indicates that the presence of oxygen vacancies (consequently increasing the surface Ce^{3+}/Ce^{4+}) results in decreasing the charge transfer or oxidation of TMB. In the ceria-TMB system, charge transfer is carried out from the NH_2 groups of TMB to the ceria slab. The charge is not localised on nearby cerium ions, but the excess charge is uniformly distributed across the surface. This observation is consistent with the electron sponge effect postulated by Cafun *et al.* while studying the catalytic decomposition of hydrogen peroxide over ceria surfaces.[73] It was reported that the redox partner is not a local cerium site, and the electron density is delocalised over the surface atoms during the catalytic decomposition reaction.

Furthermore, it is noted from Table 1 that the charge transfer is enhanced in the presence of fluoride ions which clearly indicates that F^- ions directly facilitate the charge transfer. Interestingly, the charge transfer in the presence of F^- ions is similar for both stoichiometric and defective ceria, suggesting a strong influence of F^- ions in the oxidation of TMB irrespective of the initial oxidation state of nanoceria which is also observed in the experimental results. Our calculations clearly elucidate that (a) the oxidation of TMB proceeds *via* charge transfer from TMB to the ceria surface and (b) the charge transfer increases in the presence of fluoride ions.

We also analyzed the ability of nanoceria to detect fluoride ions in real samples. This was achieved by analysis of the fluoride concentration in toothpaste using CeO-SC. A commercial toothpaste, with a fluoride concentration in the range of ~1000 ppm was dissolved in water and filtered to remove solid residual impurities and diluted to below detection limit concentration. The sample was spiked with different concentrations of fluoride in the range of 1–5 ppm. The detection of fluoride was achieved

Table 1 Bader charge transfer analysis to understand the effect of surface Ce^{3+}/Ce^{4+} oxidation states on the charge transfer from TMB in the presence and absence of fluoride (showing charge for two adsorbed molecules of TMB)

Structure	Charge of ceria/$\lvert e \rvert$ (Bader)
Perfect ceria/defective ceria (2 O_{vac})	0
Perfect ceria + TMB	−0.174
Perfect ceria + TMB + $2F^-$	−0.534 (Fully relaxed) −0.324 (Selective dynamics, 5 Å F^-–Ce^{4+} distance)
Defective ceria + TMB	−0.084
Defective ceria + TMB + $2F^-$	−0.513 (Fully relaxed) −0.346 (Selective dynamics, 5 Å F^-–Ce^{4+} distance)

following a similar protocol described above and the results are presented in the ESI-7a.† A concentration dependent increase in the absorbance of the samples was observed at 652 nm, suggesting that the residual fluoride can be detected by CeO-SC, in real samples. The toothpaste samples were further directly diluted to achieve fluoride concentration in a similar range (without spiking) and were detected by CeO-SC (ESI-7b†).

Biosensing of glutathione

The oxidase-like activity of nanoceria was further utilised for the development of an assay for quantitative determination of a biomolecule – glutathione, a cancer biomarker. We also explored the use of F^- ions as a signal enhancer in this assay to increase its detection range. Glutathione is a thiol group-containing amino acid responsible for maintaining cellular redox homeostasis. Glutathione generally exists in two states, reduced (GSH) and oxidised (GSSG), and maintains redox homeostasis through a dynamic equilibrium between its oxidised disulphide form and reduced free thiol groups. Healthy cells generally possess a ratio of >100 for GSH/GSSG; however, a ratio of 1 to 10 indicates the oxidative stress in cells.[74,75] Cancer cells express elevated glutathione levels to suppress the excessive reactive oxygen species (ROS) generated due to the excessive proliferation and metabolic activity of cancer cells.[76,77] Thus, the detection of glutathione *via* appropriate assays using various nanomaterials has gained significant attention in recent years[78] as a cancer detection method. Due to its broad antioxidative action, glutathione can prevent the oxidation of TMB by nanoceria. A reduction in the oxidation of TMB by nanoceria is directly proportional to the amount of glutathione and can be used as an indirect assay for its sensitive detection.

Fig. 6a shows the glutathione concentration-dependent decrease in TMB oxidation by 500 μM CeO-TH. It is observed that the addition of glutathione shows a proportional decrease in the absorbance from oxidized TMB and the addition of as low as 1 ppm glutathione results in a measurable reduction in the absorbance. A good linear detection of glutathione was observed from 1–20 ppm by endpoint absorbance analysis (Fig. 6b). However, it is also noted from Fig. 6a that the absorbance from oxidized TMB is totally quenched after the addition of 20 ppm of glutathione, thereby decreasing the higher range in which glutathione can be detected. It is noted that the cellular glutathione concentration is typically in the range of 1–2 mM.[79] Thus, detection of glutathione at a higher concentration range is equally important. Based on the knowledge that the addition of F^- ions can boost the oxidase activity of nanoceria, we explored the effect of the addition of 1 ppm fluoride ions to this assay. Fig. 6c shows the glutathione concentration-dependent decrease in the TMB oxidation by CeO-TH in the presence of 1 ppm fluoride ions. It is noted that the addition of 1 ppm F^- ions increases the TMB oxidation, thus, a higher concentration of glutathione is now required to quench the

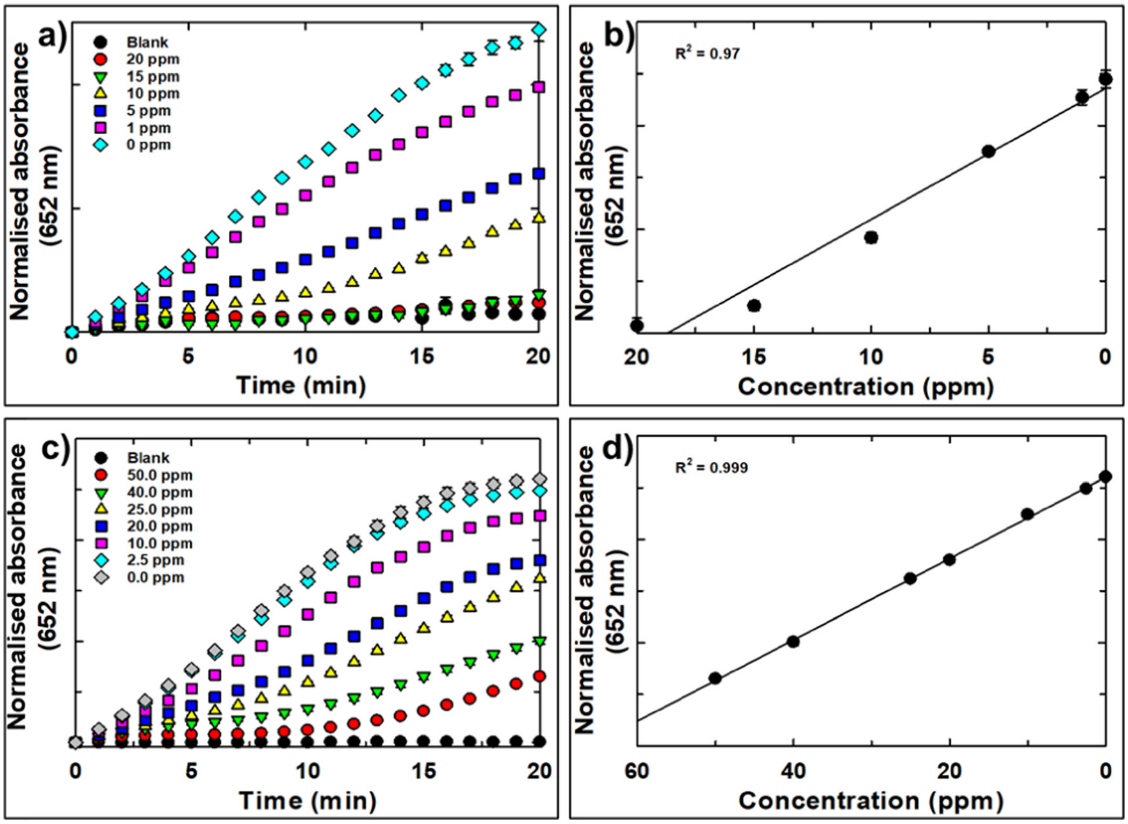

Fig. 6 Glutathione concentration-dependent decrease in the oxidation of TMB by (a) CeO-TH, (b) linear range of detection; decrease in TMB oxidation by glutathione, (c) in the presence of 1 ppm fluoride and (d) its linear range of detection.

oxidation of TMB. The use of fluoride ions in this assay increased the linear range of detection of glutathione to 50 ppm (Fig. 6d). The limit of detection (LOD) of glutathione in the presence of F^- ions, calculated by the 3σ/slope method (where σ denotes the standard deviation of the background variation) is 3.8 ppm with a linear detection range of 2.5–50 ppm. This demonstrates that fluoride ions can be used to increase the linear range of detection of glutathione in the higher concentration regime.

Summary

This study has highlighted the effect of the oxidation state of surface cerium ions of nanoceria on its oxidase mimetic activity as well as the role of F^- ions in boosting this activity. Nanoceria was synthesized using three different synthesis protocols resulting in particles with three different surface Ce^{3+} concentrations varying from ∼66% to 10%. It was demonstrated that the CeO-RT with a higher surface Ce^{3+} concentration is oxidase inactive, and a slight increase in the concentration of surface Ce^{3+} ions in CeO-SC can quickly diminish the high oxidase activity demonstrated by CeO-TH with higher surface Ce^{4+} ions. DFT calculations coupled with Bader charge analysis showed that the charge transfer from TMB to the nanoceria surface is higher in the case of stoichiometric cerium oxide surfaces than that in non-stoichiometric surfaces. It was found that F^- ions increased the charge transfer from TMB to cerium oxide irrespective of the initial surface cerium ion distribution. XPS calculations showed that the addition of up to 4 ppm of F^- ions does not change the surface Ce^{3+}/Ce^{4+} ratio in both CeO-SC and CeO-TH. Thus, contrary to previous reports, this study demonstrated that the ratio of surface Ce^{3+}/Ce^{4+} ions on the surface controls the oxidase activity as well as the degree to which F^- ions can increase the oxidase activity. Both CeO-SC and CeO-TH samples were able to detect F^- ions in water. CeO-SC with a higher surface Ce^{3+} concentration was able to detect F^- ions in a wider concentration range of 1–10 ppm as compared to 0.5–2 ppm for CeO-TH. The oxidase activity of nanoceria was also used to design a glutathione sensor and it was shown that the F^- ions can be used in this assay to detect glutathione in a wider concentration range of 2.5–50 ppm. These results show that a combination of optimum surface Ce^{3+}/Ce^{4+} ratio and F^- ion concentration can be used to selectively sense a range of analytes in a wider concentration range.

Conflicts of interest

There are no conflicts to declare.

Acknowledgements

The authors acknowledge the Technical and Scientific Assistance of Mr Bhavya Mod and Sydney Microscopy & Microanalysis, the University of Sydney node of Microscopy Australia.

References

1 S. Ayoob and A. K. Gupta, *Crit. Rev. Environ. Sci. Technol.*, 2006, **36**, 433–487.
2 S. Mukherjee, M. Shah, K. Chaudhari, A. Jana, C. Sudhakar, P. Srikrishnarka, M. R. Islam, L. Philip and T. Pradeep, *ACS Omega*, 2020, **5**, 25253–25263.
3 A. Aoun, F. Darwiche, S. Al Hayek and J. Doumit, *Prev. Nutr. Food Sci.*, 2018, **23**, 171–180.
4 M. Rizzu, A. Tanda, C. Cappai, P. P. Roggero and G. Seddaiu, *Sci. Total Environ*, 2021, **787**, 147650–147662.
5 M. Filipovic, H. Laudon, M. S. McLachlan and U. Berger, *Environ. Sci. Technol.*, 2015, **49**, 12127–12135.
6 A. K. Venkatesan and R. U. Halden, *J. Hazard. Mater.*, 2013, **252**, 413–418.
7 Y.-C. Chen, S.-L. Lo and J. Kuo, *Water Res.*, 2011, **45**, 4131–4140.
8 A. Szmagara and A. Krzyszczak, *J. Geochem. Explor.*, 2019, **202**, 27–34.
9 E. A. Martinez-Mier, J. A. Cury, J. R. Heilman, B. P. Katz, S. M. Levy, Y. Li, A. Maguire, J. Margineda, D. O'Mullane, P. Phantumvanit, A. E. Soto-Rojas, G. K. Stookey, A. Villa, J. S. Wefel, H. Whelton, G. M. Whitford, D. T. Zero, W. Zhang and V. Zohouri, *Caries Res.*, 2011, **45**, 3–12.
10 M. Kovács, R. Magarini and P. Halmos, *Toxicol. Environ. Chem.*, 2009, **91**, 1217–1227.
11 J. Tao, P. Zhao, Y. Li, W. Zhao, Y. Xiao and R. Yang, *Anal. Chim. Acta*, 2016, **918**, 97–102.
12 Y. H. Cheng, D. Barpaga, J. A. Soltis, V. Shutthanandan, R. Kargupta, K. S. Han, B. P. McGrail, R. K. Motkuri, S. Basuray and S. Chatterjee, *ACS Appl. Mater. Interfaces*, 2020, **12**, 10503–10514.
13 I. S. Turan, O. Seven, S. Ayan and E. U. Akkaya, *ACS Omega*, 2017, **2**, 3291–3295.
14 S. Juanjuan, W. Linlin and H. Yangfeng, *Anal. Methods*, 2019, **11**, 2585–2590.
15 H. Wu, Y. Li, X. He, L. Chen and Y. Zhang, *Spectrochim. Acta, Part A*, 2019, **214**, 393–398.
16 S. Swami, N. Sharma, A. Agarwala, V. Shrivastava and R. Shrivastava, *Mater. Today: Proc.*, 2021, **43**, 2926–2932.
17 X. Chen, S. Yu, L. Yang, J. Wang and C. Jiang, *Nanoscale*, 2016, **8**, 13669–13677.
18 X. Wu, H. Wang, S. Yang, H. Tian, Y. Liu and B. Sun, *ACS Omega*, 2019, **4**, 4918–4926.
19 D. Udhayakumari, *Spectrochim. Acta, Part A*, 2020, **228**, 117817–117850.
20 T. M. Inerbaev, S. Seal and A. E. Masunov, *J. Mol. Model.*, 2010, **16**, 1617–1623.
21 M. Molinari, A. R. Symington, D. C. Sayle, T. S. Sakthivel, S. Seal and S. C. Parker, *ACS Appl. Bio Mater.*, 2019, **2**, 1098–1106.
22 C. Gunawan, M. S. Lord, E. Lovell, R. J. Wong, M. S. Jung, D. Oscar, R. Mann and R. Amal, *ACS Omega*, 2019, **4**, 9473–9479.
23 T. M. Inerbaev, A. S. Karakoti, S. V. Kuchibhatla, A. Kumar, A. E. Masunov and S. Seal, *Phys. Chem. Chem. Phys.*, 2015, **17**, 6217–6221.

24 M. S. Lord, J. F. Berret, S. Singh, A. Vinu and A. S. Karakoti, *Small*, 2021, **17**, 2102342–2102364.

25 A. Dhall and W. Self, *Antioxidants*, 2018, **7**, 97–110.

26 C. Korsvik, S. Patil, S. Seal and W. T. Self, *Chem. Commun.*, 2007, 1056–1058, DOI: **10.1039/b615134e**.

27 T. Pirmohamed, J. M. Dowding, S. Singh, B. Wasserman, E. Heckert, A. S. Karakoti, J. E. King, S. Seal and W. T. Self, *Chem Commun*, 2010, **46**, 2736–2738.

28 A. Asati, S. Santra, C. Kaittanis, S. Nath and J. M. Perez, *Angew. Chem., Int. Ed.*, 2009, **48**, 2308–2312.

29 N. Yadav, V. Patel and S. Singh, *Advances in spectroscopy: Molecules to materials*, Springer, 2019, pp. 193–213.

30 Q. Chen, C. Liang, X. Zhang and Y. Huang, *Talanta*, 2018, **182**, 476–483.

31 P. Liu, X. Li, X. Xu, X. Niu, M. Wang, H. Zhu and J. Pan, *Sens. Actuators, B*, 2021, **338**, 129866.

32 K. Ye, X. Niu, H. Song, L. Wang and Y. Peng, *Anal. Chim. Acta*, 2020, **1126**, 16–23.

33 N. R. Nirala, S. Abraham, V. Kumar, A. Bansal, A. Srivastava and P. S. Saxena, *Sens. Actuators, B*, 2015, **218**, 42–50.

34 L. Huang, D. W. Sun, H. Pu and Q. Wei, *Compr. Rev. Food Sci. Food Saf.*, 2019, **18**, 1496–1513.

35 H. Cheng, S. Lin, F. Muhammad, Y.-W. Lin and H. Wei, *ACS Sens.*, 2016, **1**, 1336–1343.

36 D. Yang, M. Fa, L. Gao, R. Zhao, Y. Luo and X. Yao, *Nanotechnology*, 2018, **29**, 385101.

37 Y. Zhao, H. Li, A. Lopez, H. Su and J. Liu, *ChemBioChem*, 2020, **21**, 2178–2186.

38 B. Liu, Z. Huang and J. Liu, *Nanoscale*, 2016, **8**, 13562–13567.

39 K. Mukhopadhyay, A. Ghosh, S. K. Das, B. Show, P. Sasikumar and U. Chand Ghosh, *RSC Adv.*, 2017, **7**, 26037–26051.

40 L. Huang, W. Zhang, K. Chen, W. Zhu, X. Liu, R. Wang, X. Zhang, N. Hu, Y. Suo and J. Wang, *Chem. Eng. J.*, 2017, **330**, 746–752.

41 Y. Wang, T. Liu and J. Liu, *ACS Applied Nano Materials*, 2019, **3**, 842–849.

42 Y. Zhao, Y. Wang, A. Mathur, Y. Wang, V. Maheshwari, H. Su and J. Liu, *Nanoscale*, 2019, **11**, 17841–17850.

43 Y. Zhao, H. Li, A. Lopez, H. Su and J. Liu, *ChemBioChem*, 2020, **21**, 2178–2186.

44 A. Karakoti, S. V. Kuchibhatla, K. S. Babu and S. Seal, *J. Phys. Chem. C*, 2007, **111**, 17232–17240.

45 S. Kuchibhatla, A. S. Karakoti, A. E. Vasdekis, C. F. Windisch, Jr., S. Seal, S. Thevuthasan and D. R. Baer, *J. Mater. Res.*, 2019, **34**, 465–473.

46 D. R. Baer, J. E. Amonette, M. H. Engelhard, D. J. Gaspar, A. S. Karakoti, S. Kuchibhatla, P. Nachimuthu, J. T. Nurmi, Y. Qiang, V. Sarathy, S. Seal, A. Sharma, P. G. Tratnyek and C. M. Wang, *Surf. Interface Anal.*, 2008, **40**, 529–537.

47 A. Sehgal, Y. Lalatonne, J.-F. Berret and M. Morvan, *Langmuir*, 2005, **21**, 9359–9364.

48 C. Slostowski, S. Marre, O. Babot, T. Toupance and C. Aymonier, *Langmuir*, 2012, **28**, 16656–16663.

49 C. Slostowski, S. Marre, J.-M. Bassat and C. Aymonier, *J. Supercrit. Fluids*, 2013, **84**, 89–97.

50 G. Kresse and J. Furthmüller, *Phys. Rev. B: Condens. Matter Mater. Phys.*, 1996, **54**, 11169–11186.

51 G. Kresse and J. Hafner, *Phys. Rev. B: Condens. Matter Mater. Phys.*, 1993, **47**, 558–561.

52 S. Dudarev, G. Botton, S. Savrasov, C. Humphreys and A. Sutton, *Phys. Rev. B: Condens. Matter Mater. Phys.*, 1998, **57**, 1505–1509.

53 P. E. Blöchl, *Phys. Rev. B: Condens. Matter Mater. Phys.*, 1994, **50**, 17953–17979.

54 T. M. Inerbaev, S. Seal and A. E. Masunov, *J. Mol. Model.*, 2010, **16**, 1617–1623.

55 C. Loschen, S. T. Bromley, K. M. Neyman and F. Illas, *J. Phys. Chem. C*, 2007, **111**, 10142–10145.

56 C. Loschen, J. Carrasco, K. M. Neyman and F. Illas, *Phys. Rev. B: Condens. Matter Mater. Phys.*, 2007, **75**(035115), 035111–035118.

57 C. Loschen, A. Migani, S. T. Bromley, F. Illas and K. M. Neyman, *Phys. Chem. Chem. Phys.*, 2008, **10**, 5730–5738.

58 D. Prieur, W. Bonani, K. Popa, O. Walter, K. W. Kriegsman, M. H. Engelhard, X. Guo, R. Eloirdi, T. Gouder, A. Beck, T. Vitova, A. C. Scheinost, K. Kvashnina and P. Martin, *Inorg. Chem.*, 2020, **59**, 5760–5767.

59 N.-W. Kim, D.-K. Lee and H. Yu, *RSC Adv.*, 2019, **9**, 13829–13837.

60 R. Zamiri, H. A. Ahangar, A. Kaushal, A. Zakaria, G. Zamiri, D. Tobaldi and J. M. Ferreira, *PLoS One*, 2015, **10**(4), e0122989.

61 V. Baldim, F. Bedioui, N. Mignet, I. Margaill and J. F. Berret, *Nanoscale*, 2018, **10**, 6971–6980.

62 D. Damatov, S. M. Laga, E. A. Mader, J. Peng, R. G. Agarwal and J. M. Mayer, *Inorg. Chem.*, 2018, **57**, 14401–14408.

63 S. Tsunekawa, J.-T. Wang, Y. Kawazoe and A. Kasuya, *J. Appl. Phys.*, 2003, **94**, 3654–3656.

64 F. Scholes, A. Hughes, S. Hardin, P. Lynch and P. R. Miller, *Chem. Mater.*, 2007, **19**, 2321–2328.

65 S. V. Kuchibhatla, A. S. Karakoti, D. R. Baer, S. Samudrala, M. H. Engelhard, J. E. Amonette, S. Thevuthasan and S. Seal, *J. Phys. Chem. C Nanomater Interfaces*, 2012, **116**, 14108–14114.

66 T. Pirmohamed, J. M. Dowding, S. Singh, B. Wasserman, E. Heckert, A. S. Karakoti, J. E. King, S. Seal and W. T. Self, *Chem. Commun.*, 2010, **46**, 2736–2738.

67 S. Singh, U. Kumar, D. Gittess, T. S. Sakthivel, B. Babu and S. Seal, *J. Biomater. Appl.*, 2021, **36**, 834–842.

68 N. V. S. Vallabani, A. S. Karakoti and S. Singh, *Colloids Surf., B*, 2017, **153**, 52–60.

69 M. I. Kim, K. S. Park and H. G. Park, *Chem Commun*, 2014, **50**, 9577–9580.

70 G. Henkelman, A. Arnaldsson and H. Jónsson, *Comput. Mater. Sci.*, 2006, **36**, 354–360.

71 Y. Jiang, J. B. Adams and M. van Schilfgaarde, *J. Chem. Phys.*, 2005, **123**, 064701.

72 N. V. Skorodumova, M. Baudin and K. Hermansson, *Phys. Rev. B: Condens. Matter Mater. Phys.*, 2004, **69**, 075401.

73 J.-D. Cafun, K. O. Kvashnina, E. Casals, V. F. Puntes and P. Glatzel, *ACS Nano*, 2013, **7**, 10726–10732.

74 S. K. Biswas and I. Rahman, *Mol. Aspects Med.*, 2009, **30**, 60–76.

75 J. Pizzorno, *J. Integr. Med.*, 2014, **13**, 8–12.

76 H. Lv, C. Zhen, J. Liu, P. Yang, L. Hu and P. Shang, *Oxid. Med. Cell. Longevity*, 2019, **2019**, 3150145.

77 J. N. Moloney and T. G. Cotter, *Semin. Cell Dev. Biol.*, 2018, **80**, 50–64.

78 R. Jia, K. Jin, J. Zhang, X. Zheng, S. Wang and J. Zhang, *Sens. Actuators, B*, 2020, **321**, 128506.

79 H. J. Forman, H. Zhang and A. Rinna, *Mol. Aspects Med.*, 2009, **30**, 1–12.